Journal of Petroleum Exploration and Production Technology (2018) 8:1413–1424
https://doi.org/10.1007/s13202-017-0417-0

ORIGINAL PAPER - PRODUCTION ENGINEERING

A 3D numerical model for investigation of hydraulic fracture configuration in multilayered tight sandstone gas reservoirs

Qi Gao[1] · Yuanfang Cheng[1] · Chuanliang Yan[1]

Received: 11 September 2017 / Accepted: 5 December 2017 / Published online: 16 December 2017

Abstract

Multilayered tight sandstone gas reservoirs with low porosity and low permeability are usually developed by two kinds of hydraulic fracturing techniques, including general fracturing (simultaneously fracturing multiple target zones) and separate layer fracturing (sequentially fracturing the target zones from the bottom-up). However, fractures from different target zones are likely to communicate in the fracturing process which detrimentally causes the waste of fracturing fluid and proppants and finally affects the efficiency of fracturing treatment. Therefore, investigation related to hydraulic fracture configurations under different fracturing stimulation treatments is necessary with the objective of optimizing the fracturing design and predicting the production rate. In this paper, a 3D finite element model is established to simulate the propagation of multiple hydraulic fractures in the vertical well, and fracture configurations under different fracturing techniques and formation properties are analyzed and compared. The results indicate that, in vertical wells, stress interference between the fracture tips will accelerate the communication of adjacent vertical fractures along the height direction. And separate layer fracturing is preferable for stimulating multilayered tight sandstone gas reservoirs. Also, adjacent pay zones and barriers with high in situ stress contrast, high tensile strength contrast and low elastic modulus contrast are able to effectively prevent the communication of fractures along the height direction and lead to the increase of fracture length and width, and so does the barriers with large thickness.

Keywords Tight sandstone gas · Multilayered reservoir · General fracturing · Separate layer fracturing · Fracture configuration · Finite element method

Introduction

Recently, multilayered tight sandstone gas reservoirs are gradually playing a more and more significant role in the oil and gas exploration and development from northeast China. This type of reservoirs exhibits challenges for development because of the following features (Fu 2006) including thin pay zones, low porosity and permeability, large in situ stress contrast between adjacent layers and low production rate. Therefore, hydraulic fracturing stimulation is necessary for economically increase the recoverable reserves underground. General fracturing and separate layer fracturing techniques are the prevalent methods for developing multilayered tight sandstone gas reservoirs; thus, investigation of the fracture configurations under these treatments should be carried out for increasing the success rate during operation.

Modeling the hydraulic fracture propagation is still a challenge at present because of the constantly moving boundaries and coupling effects among solid and fluid (Wang 2015). The coupling phenomenon can be divided into three processes, (1) fluid flow within the fracture, (2) fluid seeps from the fracture surface into formation and (3) the deformation of formation caused by formation fluid flow and pore pressure change. The complexity of the problem seriously restricts the application of classical models like KGD (Perkins and Kern 1961; Nordgren 1972) and PKN (Geertsma and De Klerk 1969; Khristianovich and Zheltov 1955) in optimizing the fracture design. Currently, the prevailing methods for simulating hydraulic fracture propagation include displacement discontinuity method (Varahanaresh and Ahmad 2015; Dharmendra and Ahmad 2016;

✉ Qi Gao
935131241@qq.com

Yuanfang Cheng
731491711@qq.com

Chuanliang Yan
1184231108@qq.com

[1] College of Petroleum Engineering, China University of Petroleum (East China), Qingdao 266580, China

Wu and Olson 2016; Zhou et al. 2015), discrete element method (Deng et al. 2014; Conny and Heinz 2015) and finite element method (Zhang et al. 2010; Wang et al. 2012, 2015; Mahdi and Kamy 2015; Gonzalez et al. 2015; Wang et al. 2016; Feng and Gray 2017a; Lee et al. 1994).

Taking the above-mentioned methods, the propagation and interaction between multiple transverse hydraulic fractures under different fracturing sequences along horizontal wellbores has been investigated by a few researchers, Fig. 1d. Wu and Olson (2016) analyzed simultaneous propagation of three fractures in one fracturing stage. Wang et al. (2016) studied the fracture geometry under sequential and alternate fracturing technique. Varahanaresh and Ahmad (2015) and Dharmendra and Ahmad (2016) simulated the conventional and modified "zipper" fracturing scenario in which two or more horizontal wellbores are involved in the stimulation treatment. The above researches were done under the circumstance that the whole calculation domain shares the same properties and the interference between fractures is mainly caused by compressive stress. Moreover, the propagation behavior of hydraulic fracture in multilayered formations has also been studied. Zhang et al. (2010) established a model to calculate the fracture shape in three layers which contains one pay zone and two barriers. Wang et al. (2015) investigated the impact of formation interface shear failure on fracture height containment. Wang et al. (2012) used a more sophisticated model involving six layers to research the fracture geometry under different formation properties. These models just considered the propagation of one single fracture, Fig. 1a and c.

However, researches on the interaction behavior between multiple vertical fractures at different depths along the vertical wells are still far not enough, Fig. 1b, especially when developing multilayered tight sandstone gas reservoirs. In this paper, a 3D fluid–solid-damage coupling model using finite element method is built to investigate the problem and fracture configurations under different fracturing techniques and formation properties are analyzed. Considering the capability of addressing the process zone ahead of the fracture tips, cohesive elements were adopted to simulate the fracture initiation and propagation process.

Mathematical and physical model

Fracture initiation and propagation

A modified cohesive zone model, namely pore pressure cohesive zone model, has been used in this study to simulate the fracture initiation and propagation behavior. Figure 2 depicts the traction–separation response of the cohesive elements. Three failure mechanisms are presented (Gonzalez et al. 2015): (1) damage initiation, which refers to the beginning of degradation; (2) damage evolution, when stress intensity factor exceeds formation toughness; and (3) complete failure which means cohesive element is no longer effective. Among various damage initiation criteria, the quadratic nominal stress criterion is adopted in this paper (Feng and Gray 2017b; Turon et al. 2006):

$$\left(\frac{\sigma_{\mathrm{n}}}{\sigma_{\mathrm{n}}^{\mathrm{o}}}\right)^2+\left(\frac{\sigma_{\mathrm{s}}}{\sigma_{\mathrm{s}}^{\mathrm{o}}}\right)^2+\left(\frac{\sigma_{\mathrm{t}}}{\sigma_{\mathrm{t}}^{\mathrm{o}}}\right)^2=1 \tag{1}$$

where σ denotes the traction on cohesive elements; σ^0 is the traction at damage initiation point; n, s, t are the normal, first shear and second shear directions, respectively. The symbol

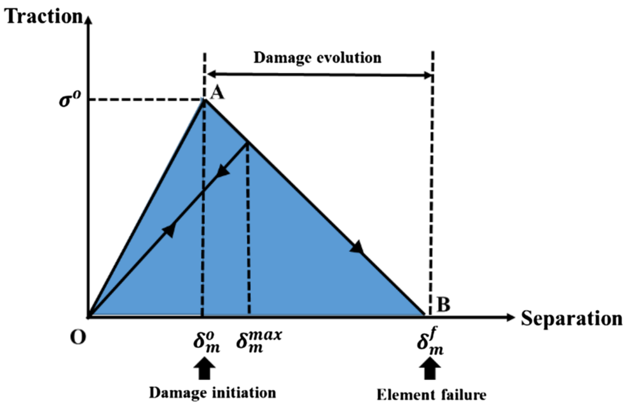

Fig. 2 Traction–separation law of bilinear displacement cohesive element

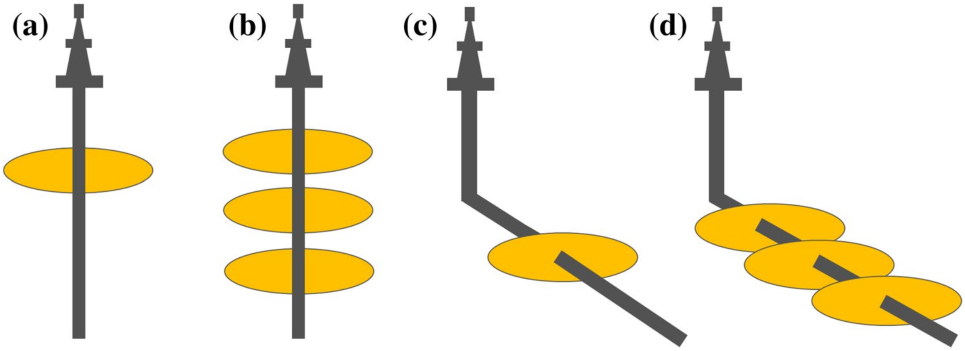

Fig. 1 Fracture propagation along vertical and horizontal wellbores

$\langle\ \rangle$ is Macaulay bracket, with common usage, representing no damage when cohesive element acts on purely compressive loads or deformation.

Cohesive layer stiffness is another parameter to determine the damage initiation feature, and it can be calculated by:

$$K_{\mathrm{coh}} = \frac{\sigma_{\mathrm{o}}}{\delta_{\mathrm{m}}^{\mathrm{o}}} = \frac{2G^{\mathrm{c}}}{\delta_{\mathrm{m}}^{\mathrm{o}}\delta_{\mathrm{m}}^{\mathrm{f}}} \tag{2}$$

where G^{c} is the critical fracture energy which equals the area surrounded by traction–separation law curve OAB and horizontal axis, and $\delta_{\mathrm{m}}^{\mathrm{o}}$ and $\delta_{\mathrm{m}}^{\mathrm{f}}$ are, respectively, the separation at the damage initiation and complete failure point. The fracture starts to propagate when $\delta_{\mathrm{m}}^{\mathrm{f}}$ is reached in every single cohesive element.

B–K model (Benzeggagh and Kenane 1996) is implemented in our work to simulate the damage evolution process during fracture propagation. This type of energy relationship is able to take all probable mixed mode damage mechanisms into consideration:

$$G_{\mathrm{n}}^{\mathrm{c}} + \left(G_{\mathrm{s}}^{\mathrm{c}} - G_{\mathrm{n}}^{\mathrm{c}}\right)\left(\frac{G_{\mathrm{s}} + G_{\mathrm{t}}}{G_{\mathrm{n}} + G_{\mathrm{s}} + G_{\mathrm{t}}}\right)^{\eta} = G^{\mathrm{c}} \tag{3}$$

where $G_{\mathrm{n}}^{\mathrm{c}}$ is the critical fracture energy in mode I, $G_{\mathrm{s}}^{\mathrm{c}}$ is the critical fracture energy in mode II, and III, G_{n}, G_{s}, G_{t} are the fracture energy in mode I, II and III, respectively, and η is a parameter related to material properties and demonstrates the contribution of shear mode ratio to critical fracture energy. In this paper, 2.28 is used for η.

Owing to the lack of experimental data and difficulties in predicting the fracturing regime, the energy release rate can be summarized into the following form (Mahdi and Kamy 2015):

$$G_i = \alpha K_i^2 1 - v^2/\mathrm{E} \tag{4}$$

where K is the mode-dependent fracture toughness, υ stands for Poisson's ratio, E represents elastic modulus, α is a factor concerning rock properties and, in this work, for pay zones and barriers it, respectively, equals 1 and 5, and i can be replaced by n, s, t depending on the fracture mode.

Fluid flow in fracture

The fluid flow in hydraulic fractures can be divided into two major types: tangential flow and normal flow, Fig. 3. Using the lubrication approximation for tangential flow process, the laminar and incompressible Newtonian fluid with viscosity μ is taken for the analysis. Also, the fluid flow channel is set to be much narrower compared to its length. The model is stated as follows (Boone and Ingraffea 1990):

$$q_{\mathrm{f}} = -\frac{w^3}{12\mu}\frac{\partial p_{\mathrm{f}}}{\partial x} \tag{5}$$

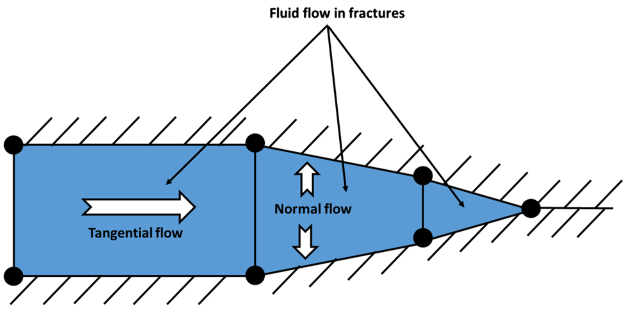

Fig. 3 Fluid flow between cohesive element faces

where q_{f} is the flow rate along the fracture length, μ is the viscosity of the fluid in the fracture, and w is the fracture opening, and p_{f} is the pressure in the fracture.

For normal flow process, pressure-dependent leak-off model is used to describe the fluid flow from fracture into the surrounding formation pores:

$$q_{\mathrm{l}} = c_{\mathrm{l}}\left(p_{\mathrm{f}} - p_{\mathrm{m}}\right) \tag{6}$$

where p_{m} is the formation pressure, q_{l} is the fluid loss from fracture into formation per unit surface area, and c_{l} is the fluid leak-off coefficient.

Coupling between fluid and rock

Hydraulic fracture propagation is such a complex physical phenomenon which involves dynamic coupling between fluid flow and rock deformation, and the theory of poroelasticity introduced by Biot (1962) can be adopted to describe the fluid and solid mechanical interaction process. In porous media saturated with fluid, the total stress is related to effective stress in this way:

$$\boldsymbol{\sigma} = \bar{\boldsymbol{\sigma}} + \alpha p_{\mathrm{m}}\boldsymbol{I} \tag{7}$$

where $\boldsymbol{\sigma}$ is the total stress matrix, $\bar{\boldsymbol{\sigma}}$ is the effective stress matrix, and α is Biot's coefficient.

The fluid flow process in the formation adopts Forchheimer's law (ABAQUS 2014), and the permeability coefficient is defined as:

$$\bar{k} = \frac{k_{\mathrm{s}}}{\left(1 + \beta\sqrt{v_{\mathrm{w}}v_{\mathrm{w}}}\right)}k \tag{8}$$

where v_{w} is the fluid velocity; k is the permeability coefficient when formation is completely saturated; k_{s} is determined by fluid saturation S_{r}, and the relationship of the two factors can be expressed by $k_{\mathrm{s}} = S_{\mathrm{r}}^3$; and β reflects the effect of fluid seepage velocity on permeability coefficient. The formula is reducible to Darcy law when β reaches zero.

The stress equilibrium equation of the solid formation under current configuration can be described in the form of virtual work (Wang 2015; ABAQUS 2014; Feng et al. 2017):

$$\int_V \boldsymbol{\sigma} : \delta\boldsymbol{\varepsilon} dV = \int_S \boldsymbol{t}\cdot\delta\boldsymbol{v} dS + \int_V \boldsymbol{f}\cdot\delta\boldsymbol{v} dV \tag{9}$$

where $\boldsymbol{\sigma}$ is the total stress matrix, $\boldsymbol{f}$ is the body force vector, $\boldsymbol{t}$ is the surface stress vector, $\delta\boldsymbol{v}$ is the virtual velocity vector, $\delta\boldsymbol{\varepsilon}$ is the virtual strain rate matrix, V is the solid volume, and S is the surface area controlled by traction–separation law. The displacement is set as the nodal variables by discretizing the equation with a Lagrangian formulation for the solid formation. Thus, modeling of the porous medium can be realized by means of attaching the finite element mesh to the solid phase that allows the fluid to seep through.

The continuity of reservoir fluid is governed by the equation below in which the increase rate of fluid volume stored at a point equals the rate of volume of fluid flowing into the point within the time increment (Wang 2015; ABAQUS 2014; Feng et al. 2016, 2017):

$$\frac{\mathrm{d}}{\mathrm{d}t}\left(\int_V \rho_{\mathrm{f}}\emptyset dV\right) + \int_S \rho_{\mathrm{f}}\emptyset\boldsymbol{n}\boldsymbol{q}_{\mathrm{m}} dS = 0 \tag{10}$$

where ρ_{f} is the fluid density, $\emptyset$ is the formation porosity, $\boldsymbol{n}$ is the outward normal direction of the surface S, and $\boldsymbol{q}_{\mathrm{m}}$ is the liquid velocity vector in the permeable formation. The continuity equation is integrated in time using the backward Euler approximation and discretized with finite elements using pore pressure as the variable.

Method verification

For testing the accuracy of our numerical method, propagation behavior of a single hydraulic fracture is simulated. The basic input parameters for verification are given in Table 1. Solutions from KGD (Perkins and Kern 1961; Nordgren 1972) analytical model are introduced to compare with our numerical model:

$$w_{\mathrm{fm}} = 2.36\left(\frac{q_{\mathrm{f}}^3\mu}{E'h_{\mathrm{f}}^3}\right)^{1/6} t^{1/3} \tag{11}$$

$$p_{\mathrm{fm}} = 1.09\left(E'^2\mu\right)^{1/3} t^{-1/3} \tag{12}$$

where w_{fm} is the fracture mouth opening, p_{fm} is the fluid pressure at the fracture mouth, E' is the elastic modulus of rock under plane strain condition, and h_{f} is the fracture height. Note that to make the comparison effective and reliable, the numerical model is developed in a horizontal plane under the plane strain condition. No confinement stresses and reservoir pressure are applied to the formation with the normal displacement and pore pressure of the outer boundaries fixed as zero in the whole process. During the fluid injection stage, purely viscous fluid in the laminar flow regime is injected at a constant rate through the perforation tunnel to create hydraulic fracture, and there is no fluid leak-off into the surrounding fully saturated porous media. The total number of the meshes we use in the model is 8000. From Fig. 4, it can be observed that good agreement exists between the obtained results of the established model and the KGD solutions.

Table 1 Input parameters for model verification

Input parameters			
Maximum horizontal stress (MPa)	0	Porosity	0.2
Minimum horizontal stress (MPa)	0	Elastic modulus (GPa)	20
Pore pressure (MPa)	0	Poisson's ratio	0.2
Fracture toughness (MPa m$^{1/2}$)	1.5	Injection rate (m^2/s)	1e−4
Tensile strength (MPa)	1	Fluid viscosity (mPa s)	10
Permeability (mD)	20	Fluid leak-off rate (m^2/s)	0

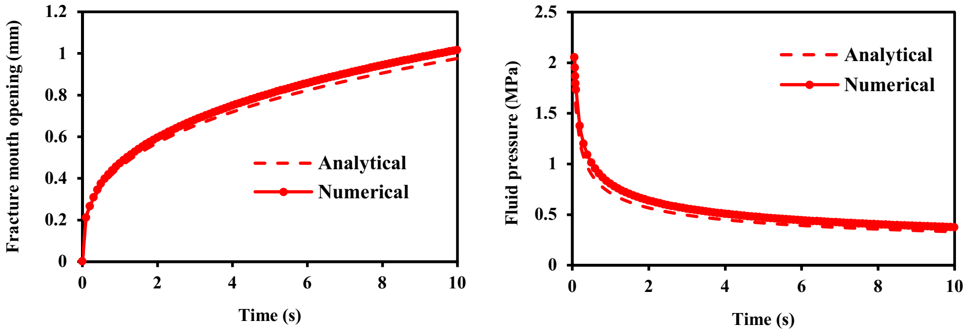

Fig. 4 Comparison between analytical and numerical solution

Finite element model description

Based on the actual geological condition in Daqing oilfield, a 200 m × 100 m × 100 m 3D finite element model is established to study the hydraulic fracture configuration when developing multilayered tight sandstone gas reservoirs. The model consists of five parts including three barriers and two pay zones. Pay zones 1 and 2 are separately sandwiched between barriers 1, 2 and 3, as depicted in Fig. 5. The minimum horizontal principal stress, maximum horizontal principal stress and overburden pressure are exerted along *X*, *Z* and *Y* directions, respectively. Two perforation tunnels are inserted into the pay zones to simulate the initiation and propagation of hydraulic fractures, and both of them are located along the vertical wellbore axis. In the whole reservoir domains, it is assumed that all of the five parts are isotropic and heterogeneous, and the interfaces between the pay zones and barriers are well bonded with no slippage occurring during the fracturing treatment. 53216 C3D8RP (8-node brick, displacement and pore pressure elements with reduced integration) elements are adopted to represent the reservoir rocks. At the outer boundaries, the displacement along the normal direction is fixed as zero with pore pressure kept as a constant equaling to the original reservoir pressure. In addition, mesh refinement is done near the fracture propagation area to ensure the accuracy of the simulation results. Basic input parameters of pay zones and barriers are listed in Table 2. Columns filled in by just one single value represent that the corresponding properties will not change in the simulation process. It also needs to be mentioned that the lowest point of the wellbore axis in Fig. 5 is set to be the reference point with the coordinate of (*X*, *Y*, *Z*) = (0, 0, 0) when doing the analysis in the following sections.

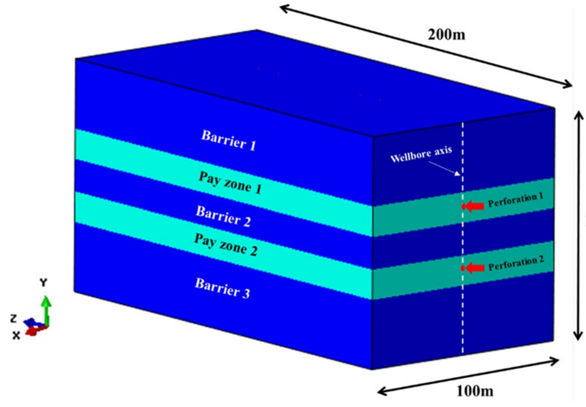

Fig. 5 Schematic diagram of hydraulic fracturing model

Fracture configuration comparison under general fracturing and separate layer fracturing

General fracturing and separate layer fracturing techniques are widely used to stimulate the multilayered tight sandstone gas reservoirs. In this work, pay zones 1 and 2 are stimulated simultaneously under general fracturing for 30 min, whereas fractures are initiated sequentially from the bottom-up each for 30 min (total 60 min) under separate layer fracturing. Herein, we define F1 and F2 to represent the created fractures in pay zone 1 and pay zone 2, respectively. The minimum horizontal principal stress at different time points during separate layer fracturing in *X*–*Y* plane is shown in Fig. 6. Figure 6a presents the configuration of F2 after fracturing for 30 min. It can be

Table 2 Reservoir conditions and basic parameters of different layers

Properties	Layers				
	Barrier 1	Pay zone 1	Barrier 2	Pay zone 2	Barrier 3
Elastic modulus (GPa)	30[a], 45, 60	25	30[a], 45, 60	25	30[a], 45, 60
Poisson's ratio	0.22	0.25	0.22	0.25	0.22
Permeability (mD)	0.05	0.2	0.05	0.2	0.05
Porosity	0.05	0.09	0.05	0.09	0.05
Pore pressure (MPa)	20	20	20	20	20
Minimum horizontal principal stress (MPa)	38.6, 41.6, 44.6[a]	34.6	38.8, 41.8, 44.8[a]	34.8	39, 42, 45[a]
Maximum horizontal principal stress (MPa)	43.6, 46.6, 49.6[a]	39.6	43.8, 46.8, 49.8[a]	39.8	44, 47, 50[a]
Overburden pressure (MPa)	55	55.25	55.45	55.65	55.9
Tensile strength (MPa)	2, 6, 10[a]	1	2, 6, 10[a]	1	2, 6, 10[a]
Injection rate (m^3/s)		0.05[a], 0.1, 0.2		0.05[a], 0.1, 0.2	
Fluid viscosity (cp)		10		10	
Layer thickness (m)	30, 27.5[a], 25	13	14, 19[a], 24	13	30, 27.5[a], 25

[a] Means that the value is used for the base case

observed that the lower fracture tip of F2 stops near the layer interface, while the upper fracture tip penetrates into the barrier 2 for a short distance. This is mainly because the initial in situ stress in barrier 2 is smaller than that in barrier 3. Also, stress concentration phenomenon occurs at the fracture tips. It is interesting to note that the stress-redistributed area shaped like a "butterfly" and, along the fracture propagation direction, the stress magnitude declines rapidly ahead of the fracture tips which will make the propagation of F1 in barrier 2 easier. At the moment of fracturing for 50 min, the stress interference in barrier 2 between F1 and F2 arises, as shown in Fig. 6b. Besides, Fig. 8a illustrates the minimum horizontal principal stress value along the wellbore axis in barriers 1 and 2 after 50-min fracturing operation. Obviously, the stress value in barrier 2 is much lower than that in barrier 1 and the stress distribution greatly influences the final geometry of F1, Fig. 6c. For further observation, the height of F1 is larger than F2.

From Fig. 7a, the stress interference phenomenon happens in barrier 2 after general fracturing only for 19 min and it is 31 min earlier compared to separate layer fracturing. The minimum horizontal principal stress distribution along the wellbore axis in barriers 1, 2 and 3 at this moment is depicted in Fig. 8b. Although the original minimum horizontal principal stress in barrier 2 is greater than that in barrier 1, the stress magnitude near the fracture tips in barrier 2 turns to be the minimum due to the stress interference between F1 and F2. Thus, the growth of two fractures in barrier 2 along height direction accelerates and the total fracture height of F1 and F2 under general fracturing for 25 min is even greater than that under separate

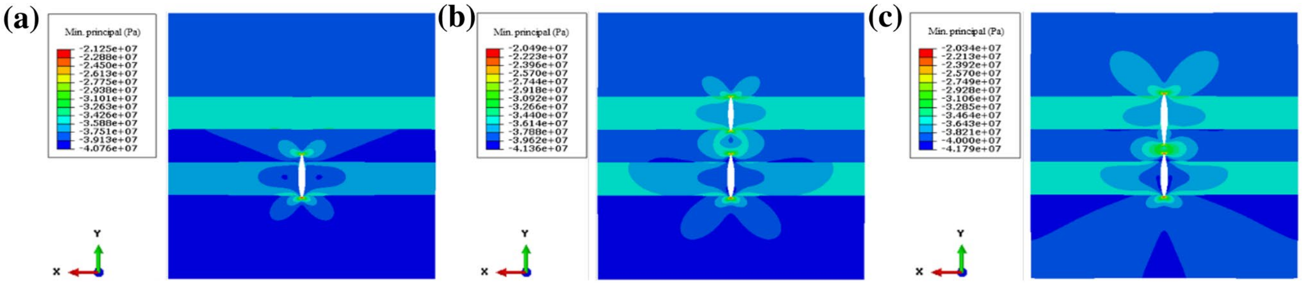

Fig. 6 Minimum horizontal principal stress distribution at different times during separate layer fracturing in *X*–*Y* plane. **a** 30 min, **b** 50 min, **c** 60 min

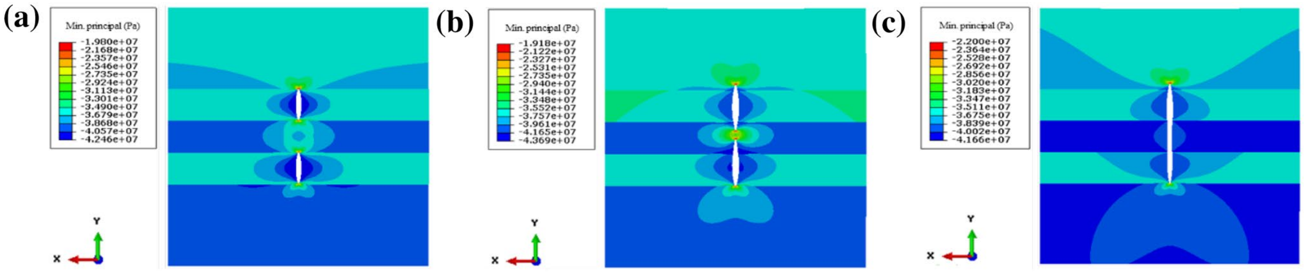

Fig. 7 Minimum horizontal principal stress distribution at different times during general fracturing in *X*–*Y* plane. **a** 19 min, **b** 25 min, **c** 30 min

Fig. 8 Minimum horizontal principal stress distribution in barriers along the wellbore axis. **a** Separate layer fracturing for 50 min, **b** general fracturing for 19 min

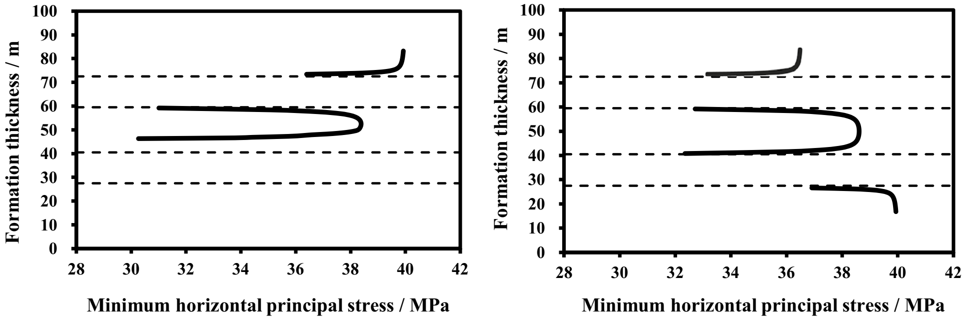

layer fracturing for 60 min. When the hydraulic fracturing is lasted for 30 min, the connection of F1 and F2 makes the whole fracture look thinner in barrier 2 and wider in the pay zones, Fig. 7c.

Figure 9 shows the variation of injection fluid pressure at the fracture mouth with time in two fracturing modes. It can be obtained from Fig. 9a that the initiation pressure of F1 is larger than that of F2 in separate layer fracturing treatment. This is mainly because the horizontal opening of F2 results in the bounding rock matrix being compressed horizontally. In response, the matrix expands vertically (Poisson's ratio effect), causing the increase of stresses around F1. Besides, the propagation pressure evolution of F1 and F2 presents similar trend, and both of them exhibit larger values at the later stage as a result of the penetration of the fractures into the barriers. From Fig. 9b, the difference of the fluid pressure in F1 and F2 can be ignored.

Based on the above analysis, we can draw the conclusion that fracture communication under general fracturing is much more likely to occur compared to separate layer fracturing. It needs to be pointed out that fracture communication can lead to the waste of fracturing fluid and proppants and negatively affect the fracturing efficiency because the fracturing fluid and proppants tend to settle into F2 under gravity, which will cause F1 unpropped and closed. Moreover, as illustrated in Fig. 10a and b, fracture communication also decreases the fracture length and width. Therefore, separate layer fracturing technique is preferable for stimulating multilayered tight sandstone gas reservoirs.

Fracture configuration under different formation properties

However, some factors may influence the performance of separate layer fracturing treatment, including in situ stress contrast between adjacent pay zones and barriers, tensile strength contrast between adjacent pay zones and barriers, elastic modulus contrast between adjacent pay zones and barriers and barrier thickness. Due to the variation of these factors, not all wells could be a good choice for separate layer fracturing. Hence, it is necessary to study the fracture configuration under different geological circumstances so that the simulation results can provide theoretical guidance for selecting candidate wells.

Effects of in situ stress contrast between adjacent pay zones and barriers

Three different in situ stress contrasts between pay zones and barriers are considered when simulating and analyzing the separate layer fracturing process. The minimum principal stress contrast is, respectively, taken as 4, 7 and 10 MPa, with other parameters keeping constant. Fracture

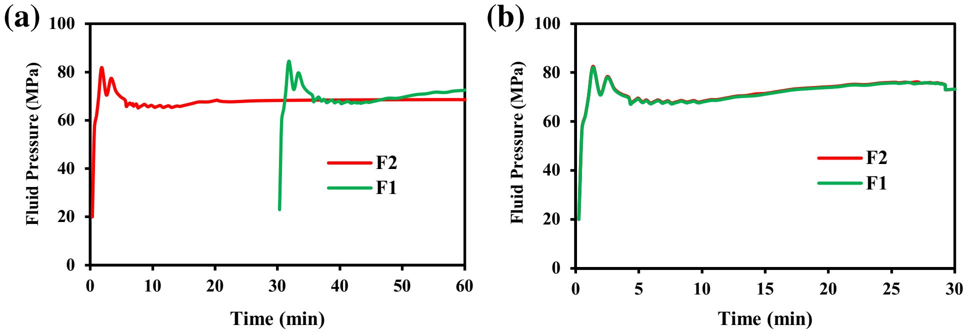

Fig. 9 Fluid pressure behavior at the fracture mouth during separate layer fracturing and general fracturing. **a** Separate layer fracturing, **b** general fracturing

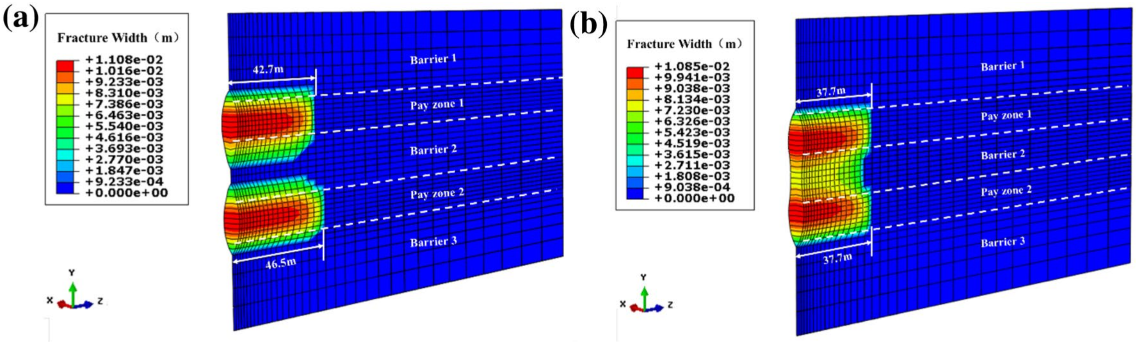

Fig. 10 3D fracture configuration at the end of fracturing treatments. **a** Separate layer fracturing for 60 min, **b** general fracturing for 30 min

configuration after fracturing for 60 min can be seen from Figs. 11 and 12. Obviously, these figures reveal a downward trend for fractures to communicate with the increase of in situ stress contrast. When the in situ stress contrast is 4 MPa, fractures experience less resistance in the height direction, which avails the fracture growth in barriers and consequently decreases the fracture length. Due to the stress interference from previously created F2 and small in situ stress contrast, communication between F1 and F2 happens in the early pumping stage. With the continuous fluid injection, the fracture width in barrier 2 turns to be larger than that in pay zones 1 and 2 at the end. When the in situ stress contrast is 7 MPa, fracture communication phenomenon happens later because of the increase of propagation resistance in the height direction, which also reduces the fracture width in barrier 2. However, the total fracture length in pay zones becomes larger compared to the last case. When the in situ stress contrast rises to 10 MPa, the expected fracture configuration that F1 and F2 are restricted to mainly propagate in the pay zones without communication occurs. Under this in situ stress state, both the fracture length and width are the largest. Generally, larger in situ stress contrast between pay zones and barriers leads to greater fracture length and width. For this model, the in situ stress contrast increases by 6 MPa; the average fracture length and width increase by 17.1 and 20.6%, respectively.

Effects of tensile strength contrast between adjacent pay zones and barriers

Remaining other properties unchanged, fracture configurations under three different tensile strength contrasts (1, 5 and 9 MPa) between pay zones and barriers are analyzed, as depicted in Figs. 13 and 14. The simulation results show that the fracture communication trend weakens as the tensile strength contrast increases. Tensile strength is the reflection of rock ability to resist damage with larger value representing strong antidamage ability. When the

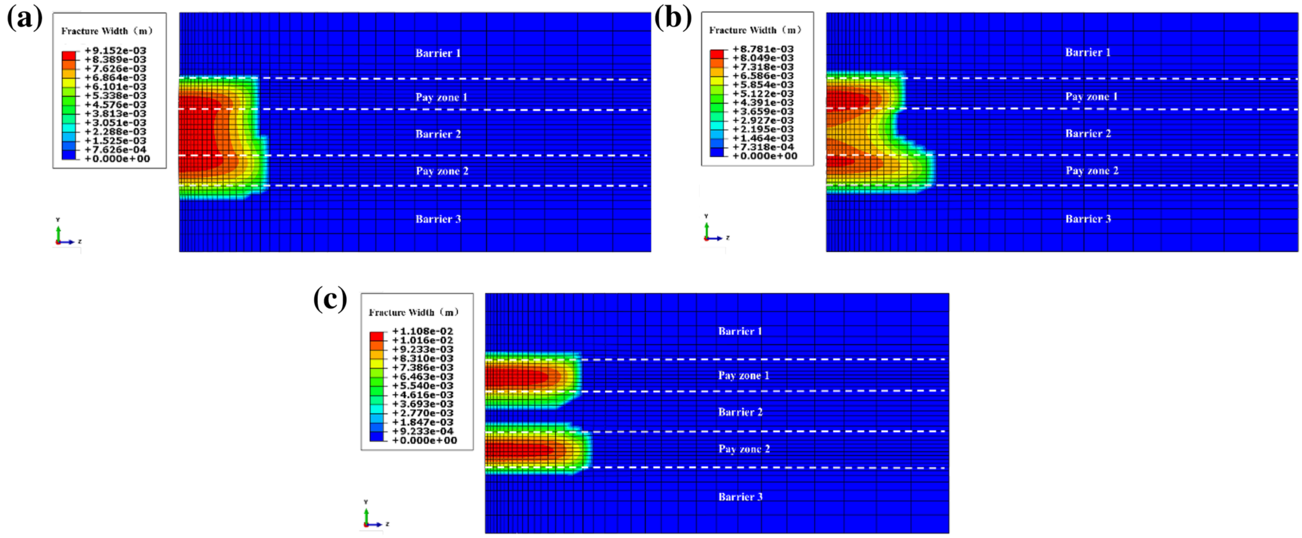

Fig. 11 Fracture configuration under different in situ stress contrasts between pay zones and barriers. **a** In situ stress contrast: 4 MPa, **b** in situ stress contrast: 7 MPa, **c** in situ stress contrast: 10 MPa

Fig. 12 Variation of fracture width and length with different in situ stress contrasts between pay zones and barriers

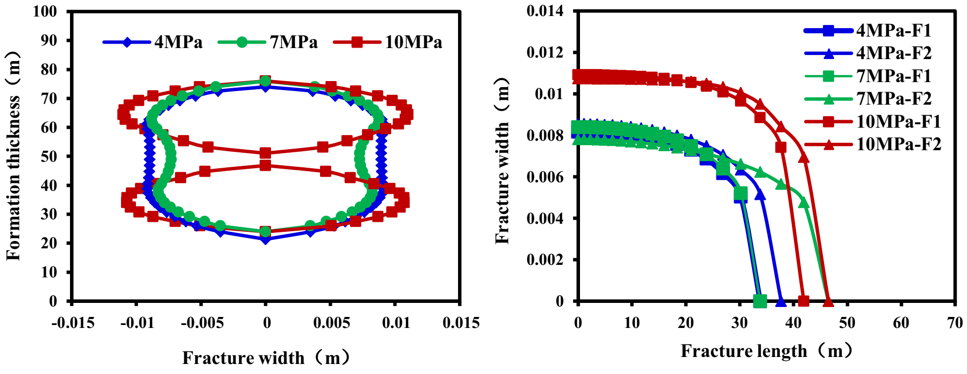

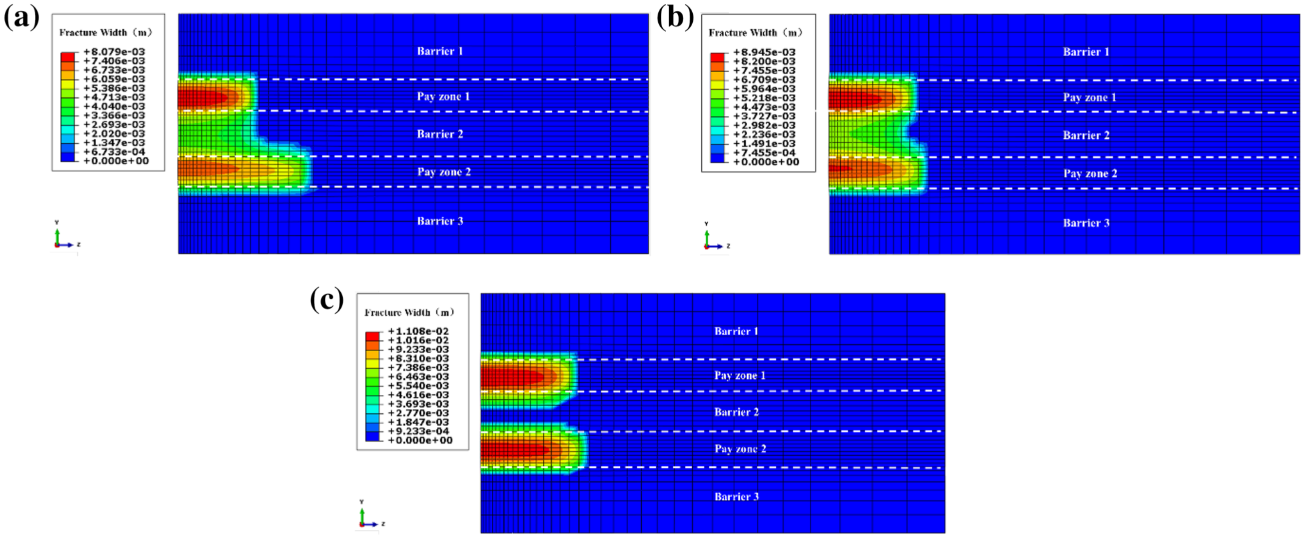

Fig. 13 Fracture configuration under different tensile strength contrasts between pay zones and barriers. **a** Tensile strength contrast: 1 MPa, **b** tensile strength contrast: 5 MPa, **c** tensile strength contrast: 9 MPa

Fig. 14 Variation of fracture width and length with different tensile strength contrasts between pay zones and barriers

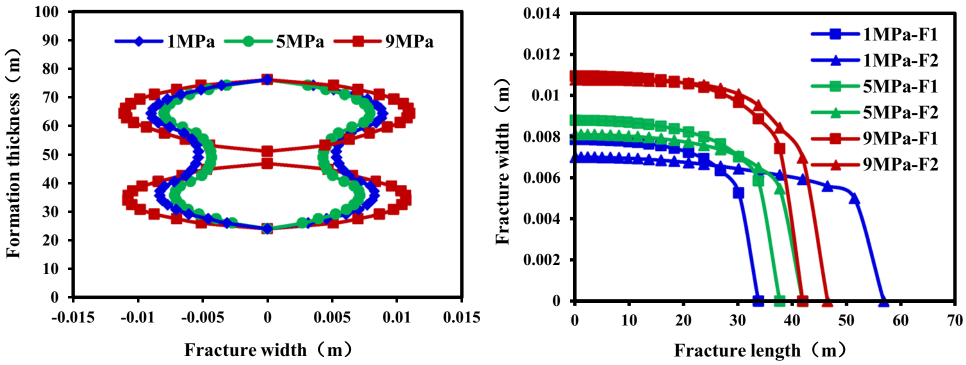

tensile strength contrast is 1 MPa, it is easier for fractures to penetrate into barrier 2 so that F1 and F2 communicate relatively earlier. It should be noted that the default in situ stress contrast is 10 MPa, which means that the opening of barrier 2 is restricted and part of the injection fluid from pay zone 1 finally contributes to the growth of F2. Hence, the length of F2 in the case is the largest in this section, while the length of F1 is the shortest. When the tensile strength contrast becomes 5 MPa, the communication of F1 and F2 still occurs, but it happens much later. Accordingly, the length of F2 decreases as F1 consumes more fracturing fluid and gets to be longer. When the tensile strength contrast increases to 9 MPa, the fracture communication phenomenon in barrier 2 disappears and consequently results in the simultaneous increase of fracture length and width. Therefore, the increased tensile strength contrasts between pay zones and barriers create better hydraulic fracture configuration. For this model, the tensile strength contrast increases by 8 MPa; the average fracture length and width increase by 14.5 and 35%, respectively.

Effects of elastic modulus contrast between adjacent pay zones and barriers

Fracture configurations influenced by three different elastic modulus contrasts are analyzed with other parameters staying the same, and the elastic modulus of barriers is, respectively, 5, 20 and 35 GPa larger than that of the pay zones. From Figs. 15 and 16, the large elastic modulus contrast leads to the communication of F1 and F2. The magnitude of elastic modulus reflects the ability of rocks to resist deformation, and the larger the elastic modulus is, the harder the rock deforms. When the elastic modulus contrast equals 5 GPa, only the top and bottom tips of fractures limitedly penetrate into the barriers, which is expected during separate layer fracturing. When the elastic modulus contrast increases to 20 GPa, the deformation extent of barriers decreases, namely

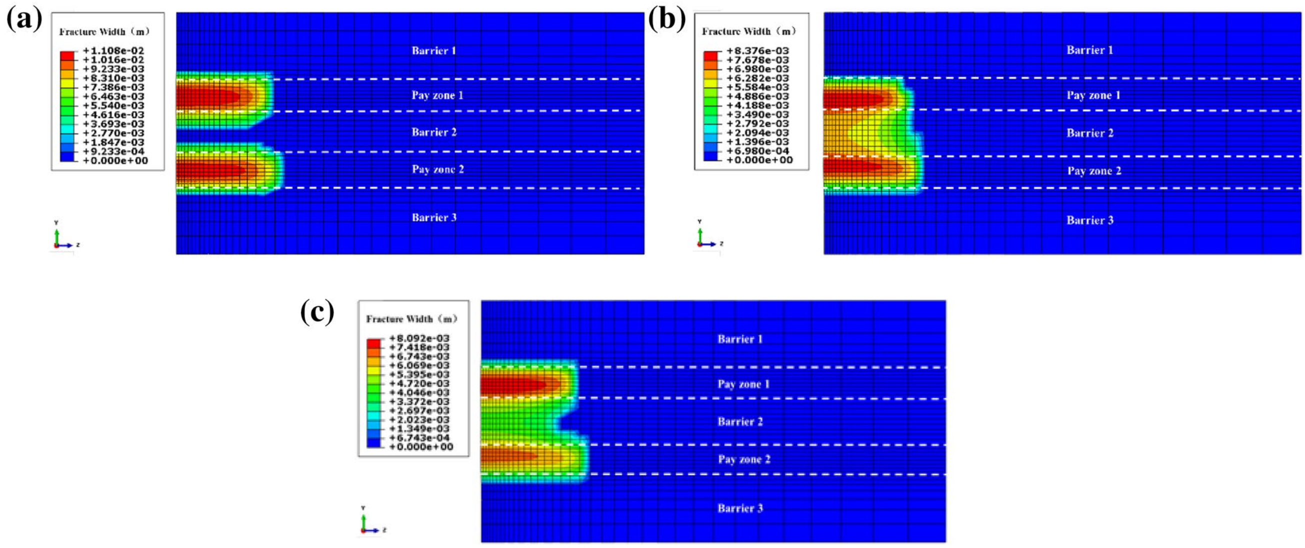

Fig. 15 Fracture configuration under different elastic modulus contrasts between pay zones and barriers. **a** Elastic modulus contrast: 5 GPa, **b** elastic modulus contrast: 20 GPa, **c** elastic modulus contrast: 35 GPa

Fig. 16 Variation of fracture width and length with different elastic modulus contrasts between pay zones and barriers

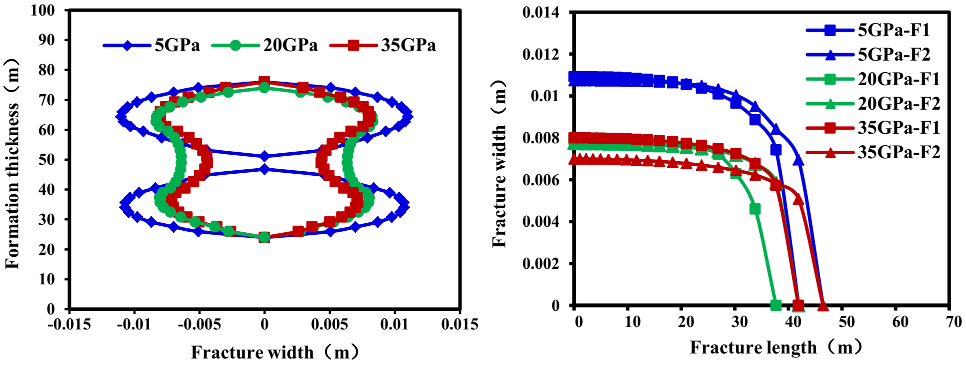

the fracture width in barriers is smaller than before. Hence, the same injected fluid volume creates narrower and shorter fractures and results in the connection of F1 and F2 in barrier 2, Fig. 15b. When the elastic modulus contrast reaches 35 GPa, the deformation of barrier 2 becomes much more difficult, which inversely increases the fracture width and length in pay zones. Thus, small elastic modulus contrast between pay zones and barriers is required to generate satisfied fracture configuration. For this model, the elastic modulus contrast increases by 30 GPa; the average fracture length and width decrease by 14.5 and 35%, respectively.

Effects of barrier thickness

Barrier thickness is also an important parameter affecting the fracturing performance. Three different thicknesses (14, 19 and 24 m) of barrier 2 are considered. The 3D fracture configurations at the end of the stimulation treatment are shown in Figs. 17 and 18. It can be concluded that larger thickness of barrier 2 efficiently reduces the probability of fracture communication. As mentioned before, the creation of F2 decreases the minimum horizontal principal stress ahead of the fracture tips along the wellbore axis direction; then, F1 will experience much less resistance to extend into the barrier 2. However, with the increase of the thickness of barrier 2, the effects from F2 on the propagation of F1 gradually disappear. When the thickness of barrier 2 is 14 m, the fracture communication occurs due to the strong stress interference between F1 and F2. When the thickness of barrier 2 is increased to 19 m, the configuration of the created two fractures can satisfy the fracturing requirement. When the thickness of barrier 2 reaches 24 m, the ideal fracture configuration that propagates only in the pay zones emerges. Thus, barriers with large thickness are beneficial for separate layer fracturing treatment, and in this model, the thickness of barrier 2 increases by 10 m; the average fracture length and width increase by 16.4 and 24.6%, respectively.

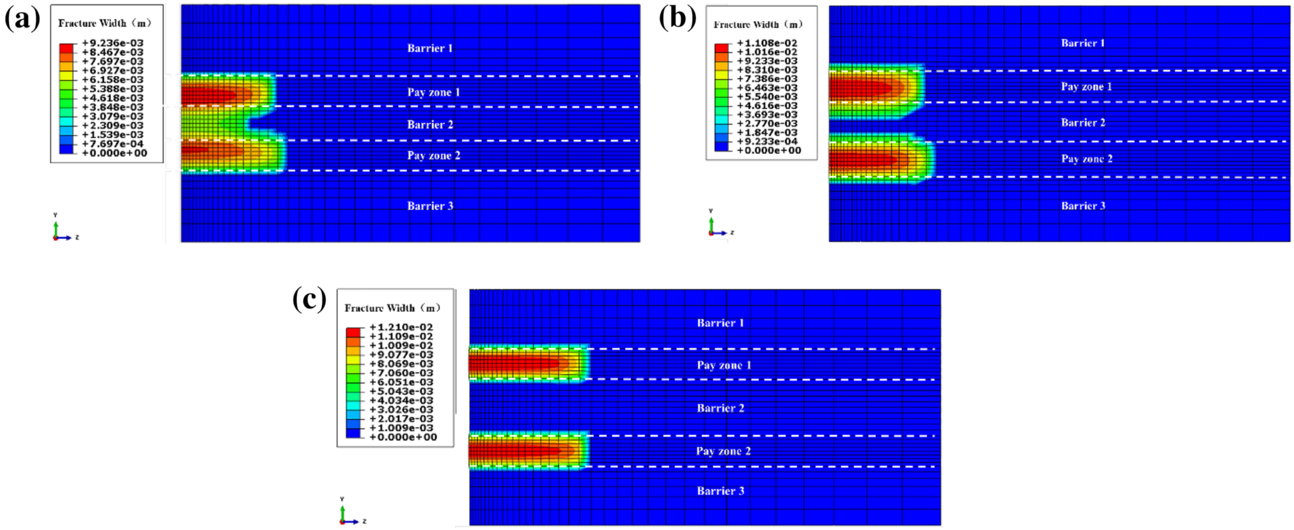

Fig. 17 Fracture configuration under different barrier thicknesses between pay zones and barriers. **a** Thickness of barrier 2: 14 m, **b** thickness of barrier 2: 19 m, **c** thickness of barrier 2: 24 m

Fig. 18 Variation of fracture width and length with different barrier thicknesses between pay zones and barriers

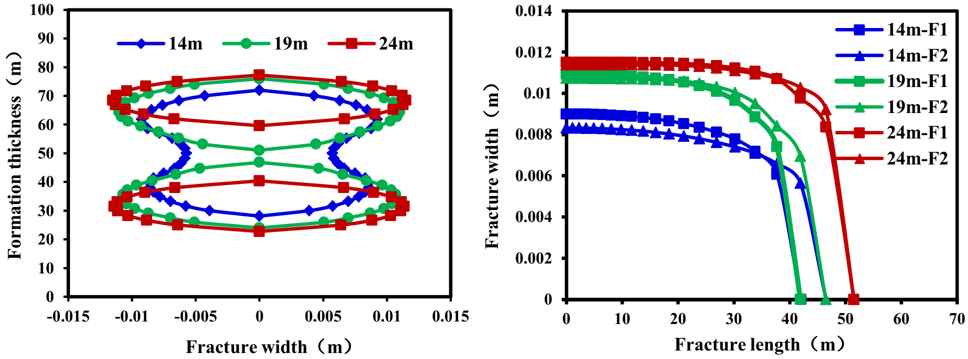

Conclusions

Even though there are a number of field fracturing treatments for multilayered tight sandstone gas reservoirs, the fundamental mechanism for fracture propagation is still not completely understood. In this paper, a 3D fluid–solid-damage coupling finite element model was established to investigate the fracture configurations under different fracturing techniques and formation properties in multilayered tight sandstone gas reservoirs. From the numerical simulation results, we can get the following conclusions.

1. In vertical wells, tensile stress-induced interference between adjacent vertical fracture tips can decrease the minimum horizontal principal stress in front of the propagation path, thus accelerating the fracture communication process.
2. Fractures are more likely to communicate under general fracturing compared to separate layer fracturing. Hence, separate layer fracturing is preferable for stimulating multilayered tight sandstone gas reservoir.
3. Adjacent pay zones and barriers with high in situ stress contrast, high tensile strength contrast, low elastic modulus contrast are able to prevent the communication of fractures along the height direction and increase the fracture length and width.
4. Barriers with large thickness are also able to prevent the communication of fractures along the height direction and increase the fracture length and width.

The presented work can provide theoretical guidance for developing multilayered tight sandstone gas reservoirs, and the model can be applied to predict the hydraulic fracture geometry in any other multilayered reservoirs with the specific formation and operation parameters.

Acknowledgement This work was supported by Program for Changjiang Scholars and Innovative Research Team in University (IRT_14R58), the National Natural Science Program (Grant Nos. 51574270 and 51504280) and the Qingdao National Laboratory for Marine Science and Technology (QNLM2016ORP0212).

References

ABAQUS (2014) ABAQUS documentation. Version 6.14

Benzeggagh ML, Kenane M (1996) Measurement of mixed-mode delamination fracture toughness of unidirectional glass/epoxy composites with mixed-mode bending apparatus. Compos Sci Technol 56:439–449

Biot MA (1962) Mechanics of deformation and acoustic propagation in porous media. J Appl Phys 33(4):1482–1498

Boone TJ, Ingraffea AR (1990) Numerical procedure for simulation of hydraulically driven fracture propagation in poroelastic media. Int J Numer Anal Methods 14(1):27–47

Conny Z, Heinz K (2015) Simulating the hydraulic stimulation of multiple fractures in an anisotropic stress field applying the discrete element method. Energy Procedia 76:264–272

Deng S, Li H, Ma G, Huang X, Li X (2014) Simulation of shale–proppant interaction in hydraulic fracturing by the discrete element method. Int J Rock Mech Min 70:219–228

Dharmendra K, Ahmad G (2016) A three-dimensional analysis of simultaneous and sequential fracturing of horizontal wells. J Pet Sci Eng 146:1006–1025

Feng YC, Gray KE (2017a) Modeling lost circulation through drilling-induced fractures. SPE J. https://doi.org/10.2118/187945-PA

Feng YC, Gray KE (2017b) Parameters controlling pressure and fracture behaviors in field injectivity tests: a numerical investigation using coupled flow and geomechanics model. Comput Geotech 87:49–61

Feng YC, Li XR, Gray KE (2017) Development of a 3D numerical model for quantifying fluid-driven interface debonding of an injector well. Int J Greenh Gas Control 62:76–90

Feng YC, Podnos E, Gray KE (2016) Well integrity analysis: 3D numerical modeling of cement interface debonding. In: Presented at the 50th U.S. Rock Mechanics and Geomechanics Symposium, Houston, Texas, 26–29 June

Fu G (2006) A new completion technology with separate layer fracturing and commingled producing in gas field. In: SPE international oil & gas conference and exhibition, 5–7 Dec, Beijing, China

Geertsma J, De Klerk F (1969) A rapid method of predicting width and extent of hydraulic induced fractures. J Pet Technol 246:1571–1581 **(SPE-2458-PA)**

Gonzalez M, Dahi Taleghani A, Olson JE (2015) A cohesive model for modeling hydraulic fractures in naturally fractured formations. In: SPE hydraulic fracturing technology conference, 3–5 Feb, The Woodlands, Texas

Khristianovich S, Zheltov Y (1955) Formation of vertical fractures by means of highly viscous fluids. In: Proceedings of the 4th world petroleum congress. Rome, Sec. II, pp 579–586

Lee TS, Advani SH, Pak CK (1994) Three-dimensional hydraulic fracture simulation using fixed grid finite element algorithms. ASME J Energy Res Technol 116(1):2906006

Mahdi H, Kamy S (2015) Simulation of hydraulic fracturing in quasi-brittle shale formations using characterized cohesive layer: stimulation controlling factors. J Unconv Oil Gas Resourc 9:65–83

Nordgren R (1972) Propagation of vertical hydraulic fractures. J Pet Technol 253:306–314 **(SPE-3009-PA)**

Perkins T, Kern L (1961) Widths of hydraulic fractures. J Pet Technol Trans AIME 222:937–949

Turon A, Camanho PP, Costa J, Dávila CG (2006) A damage model for the simulation of delamination in advanced composites under variable-mode loading. Mech Mater 38(11):1072–1089

Varahanaresh S, Ahmad G (2015) A numerical study of sequential and simultaneous hydraulic fracturing in single and multi-lateral horizontal wells. J Pet Sci Eng 132:65–76

Wang HY (2015) Numerical modeling of non-planar hydraulic fracture propagation in brittle and ductile rocks using XFEM with cohesive zone method. J Pet Sci Eng 135:127–140

Wang H, Liu H, Wu HA, Zhang GM, Wang XX (2012) A 3D nonlinear fluid–solid coupling model of hydraulic fracturing for multilayered reservoirs. Pet Sci Technol 30(21):2273–2283

Wang H, Liu H, Wu HA, Wang XX (2015) A 3D numerical model for studying the effect of interface shear failure on hydraulic fracture height containment. J Pet Sci Eng 133:280–284

Wang XL, Liu C, Wang H, Liu H, Wu HA (2016) Comparison of consecutive and alternate hydraulic fracturing in horizontal wells using XFEM-based cohesive zone method. J Pet Sci Eng 143:14–25

Wu K, Olson JE (2016) Mechanisms of simultaneous hydraulic-fracture propagation from multiple perforation clusters in horizontal wells. SPE J 21(03):1000–1008

Zhang GM, Liu H, Zhang J, Wu HA, Wang XX (2010) Three-dimensional finite element simulation and parametric study for horizontal well hydraulic fracture. J Pet Sci Eng 72:310–317

Zhou DS, Zheng P, Peng J, He P (2015) Induced stress and interaction of fractures during hydraulic fracturing in shale formation. ASME J Energy Res Technol 137(1):062902